Geophysical Research Letters

Supporting Information for

Low-Fe(III) Greenalite Was a Primary Mineral from Neoarchean Oceans

Jena E Johnson[a,1], Janet R Muhling[b,c], Julie Cosmidis[a,2], Birger Rasmussen[c], Alexis S Templeton[a]

[a]Dept. of Geosciences, University of Colorado - Boulder, 2200 Colorado Ave, Boulder CO 80309
[b]School of Earth Sciences, The University of Western Australia, 35 Stirling Highway, Crawley WA 6009, Australia
[c]Dept. of Applied Geology, Curtin University, Kent Street, Bentley, Perth WA 6102, Australia
[1]*Currently* Dept. of Earth and Environmental Sciences, University of Michigan, Ann Arbor 48109
[2]*Currently* Dept. of Geosciences, Pennsylvania State University, University Park, PA 16802

Contents of this file

Introduction

Below we detail the methods used to acquire our bulk, microscale, and nanoscale analyses of the iron silicate nanoparticle inclusions, and more fully describe the results we obtained. We present supplemental figures and supplemental tables showing results reported in the main text.

Text S1.

Methods

Thick section billets of ABDP9 380.8 m and GKF 357.5 m were drilled using a Dremel power drill to generate bulk powders of their ferruginous cherts; these powders were analyzed using bulk diffraction and spectroscopic techniques. Thin sections were also prepared from these two samples, as well as from ABDP9 222.7 m, GKF 356.6 m, and DDH44 388.3 m, to be examined optically and spectroscopically. Focused Ion Beam (FIB)-prepared foils for nanoscale analyses were produced from nearby well-preserved samples (ABDP9 219.3 m and 288.2 m, and GKF 327.2 m) from the same Western Australian and South African cores, and from the Silvergrass core at 313.6 m.

Several iron silicate standards were obtained and analyzed to compare to the ancient nanoparticle inclusions. S. Guggenheim (University of Illinois, Chicago) kindly contributed a greenalite standard from the San Valentin Ore Body, Murcia, Spain (Guggenheim et al. 1982). A minnesotaite [$Fe^{2+}_3Si_4O_{10}(OH)_2$] standard from Bluebell Mine, Riondel, Canada, analyzed by Fe XANES and STEM, was acquired from Excalibur Mineral Corporation. G. Rossman (California Institute of Technology) helpfully provided a cronstedtite standard from Kisbanya, Hungary from the Caltech Mineralogical Collection. All standards were confirmed by X-ray diffraction (XRD) and all other standards shown were derived from the JADE XRD database or the RRUFF online database.

Bulk powders were examined using XRD on a Siemens D500 X-ray diffractometer at the United States Geological Survey in Boulder. The powders were suspended in ethanol and pipetted onto a silicon wafer to form a thin layer, and then dried under gentle heating using a slide warmer. The samples were analyzed from 5 to 65 degrees two theta using Cu Kα X-ray radiation, with a step size of 0.02 degrees and a dwell time of 2 seconds per step. Jade software (MDI, version 9) and the International Centre for Diffraction Data (ICDD) 2001 database were used to identify the sample mineralogy, along with acquired standards.

At the Stanford Synchrotron Radiation Lightsource (SSRL), we obtained Fe X-ray absorption near edge spectroscopy (Fe XANES) data at Beam Line 4-1 to investigate the Fe speciation of the bulk powders and obtain the Fe XANES from standards under similar conditions as our samples. We used a Si(220) phi=90 monochromator crystal set with the beam 45% detuned. A Fe^0 foil was used for calibration with the first derivative inflection set to 7112 eV. Samples were kept in a He-filled sample chamber to maximize signal and decrease any potential Fe oxidation and a PIPS detector was used to collect fluorescence data from 6882 to 7505 eV with a 0.5 s dwell time. No change in XANES shape or position was seen over 3 repeat scans, which indicated that no oxidation was occurring. Data were collected at higher energy resolution through the Fe pre-edge and edge features (0.4 eV resolution from 7092 to 7108 eV; 0.1 eV resolution from 7108 to 7118 eV; and 0.35 eV resolution from 7118 to 7142 eV). Duplicate spectra were collected and averaged, and then normalized using Sam's Interface for XAS Package (SIXPACK) (Webb 2005).

Thin sections were examined using optical microscopy and synchrotron X-ray-based fluorescence mapping and microscale Fe μXANES. Regions of well-preserved chert were chosen and imaged using reflected and transmission light microscopy on a Zeiss stereomicroscope. X-ray fluorescence maps were then produced from these areas with an X-ray microprobe at Beam Line 2-3 at SSRL. The incident x-rays were set at 11 keV or 8eV, and the beam was focused to approximately 3x3 μm using Kirkpatrick Baez mirrors. Fluorescence data were collected using a Vortex SII International Silicon drift detector, and selected regions of interest in the fluorescence spectra were integrated over each pixel to generate images of S, K, Ca, Ti, Cr, Fe, Mn, Co, Ni, Cu, and Zn. The Fe fluorescence maps were used to choose pixels to collect full Fe XANES spectra, collected on the same beam line using a Si(220) phi=0 and Si(111) phi=0 double crystal monochromator. Spectra were measured from 6882 eV to 7505 eV at the same high resolution through the edge feature as used on Beam Line 4-1. Dwell times were set to 1 s, except for through the pre-edge feature: with the 220 crystal set, the pre-edge feature was measured with a dwell time of 5 s, while the 110 crystal set allowed greater fluorescence flux and only needed a 3 s dwell time through the pre-edge feature. These spectra were normalized and averaged using the SIXPACK software, using a linear fit to the pre-edge region and a quadratic fit to the post-edge region to normalize to an edge step height of 1, and compared to standards as mineralogical fingerprints.

We additionally analyzed the Fe pre-edge feature, located about 15-20 eV before the absorption maximum, for each μXANES spot analysis. The Fe pre-edge is related to the 1s electron transitioning to

3d or 4p orbitals. Because the pre-edge feature reflects the iron coordination environment and redox state, it can be used to approximate Fe(III)/Fe_{Total} ratios. The pre-edge features of internal standards (siderite, olivine, staurolite, cronstedtite, and chlorite standards provided by F. Bourdelle) run at the same time as the samples were used to compare against ~3x3 µm point spectra of nanoparticle-rich chert.

Small areas of polished thin sections of iron-silicate nanoparticles encased in chert were selected for synchrotron transmission X-ray microscopy (STXM) and transmission electron microscopy (TEM) analyses. FIB techniques were used to prepare ~100 nm thick foils using a *FEI Helios NanoLab G3 CX DualBeam* instrument located at the Centre for Microscopy, Characterisation and Analysis, the University of Western Australia. The selected sample areas were first coated with a strip of Pt ~1 µm thick to protect the surface, then trenches ~7 µm deep were milled on either side of the strip using a Ga ion beam with 30 kV voltage and 9.3 nA current. The foil was then cut away from the sample and welded to a Cu TEM grid. The foils were thinned with the Ga ion beam at 30 kV and 0.79 and 0.23 nA, before cleaning at 5 kV and 41 pA, and polishing at 2 kV and 23 pA.

At beamline 10ID-1 (SM) at the Canadian Light Source, we measured the iron redox state at a nanoscale using STXM. The STXM beam size was focused to 30 nm x 30 nm using a Fresnel zone plate objective and an order-sorting aperture, and the monochromator was calibrated using the 3p Rydberg peak in gaseous CO_2 at 294.96 eV. After samples were loaded, the chamber was evacuated to 0.2 Torr and then filled with He to ~127 Torr (~0.17 atm) to minimize beam absorption. We collected absorption at a 30nm or 35nm resolution to form images at 700 eV, 708 eV, 710 eV, and 718 eV. Over a subregion of the FIB foil, we additionally acquired image stacks with a 35-60 nm spatial resolution through the iron $L_{2,3}$ edge (690 – 730 eV) to generate an average spectrum for each sample. These spectra were generated with a 0.79 eV step size from 690 to 705 eV, a high energy resolution of 0.1 eV through the L_2 edge from 705 to 713 eV, a 0.19 eV step size from 713 to 719, a 0.15 eV step size from 719 to 726, and a 0.5 eV step size from 726.5 to 730 eV. Spectra from each sample were obtained from the image stacks following Cosmidis and Benzerara (2014), using the masking function in Axis2000 to only select the Fe-silicate nanoparticles and applying a linear and double arctan background correction to form a linear baseline for both L_2 and L_3 peaks.

The multiple energy absorption maps and image stacks were used to produce iron redox maps and to calculate average Fe(III)/Fe_{Total} contents from subsets of sample particles. The four full-foil absorption images were converted to optical density (OD) images, and the aXis2000 software (Hitchcock 2014) was used to calculate the iron redox state of each pixel using the method established by Bourdelle et al (2013). First, background corrections were applied by subtracting the OD image at 700 eV from both OD images at 708 eV (energy of the maximum absorption of Fe(II) at the L_3 edge) and 710 eV (energy of the maximum absorption of Fe(III) at the L_3 edge). A second correction was administered by subtracting the 718 eV OD image from the background-corrected 710 eV OD image. Subsequently, the corrected 710 eV map was divided by the corrected 708 eV map using the ratio function in aXis2000 to produce a Fe(III)/Fe_{Total} image calibrated for iron silicates by Bourdelle et al (2013). The background was masked to appear black using the masking function in aXis2000.

STXM analyses were performed first to ensure that the TEM electron beam did not alter the iron redox state, and then the same FIB foils were examined by scanning-TEM (STEM). Data were obtained at 200 kV using a *FEI Titan G2 80-200* TEM/STEM with *ChemiSTEM* technology located at the Centre for Microscopy, Characterisation and Analysis, the University of Western Australia. High-resolution TEM (HRTEM) was used to confirm the identity of the particles differentiated by HAADF and EDS data, and to

check for beam damage in the particles. No formation of a secondary amorphous layer, which could affect Fe redox state measured by STXM, was detected along edges of particles and therefore iron redox data acquired by STXM is considered to reflect the original iron silicate Fe(III)/Fe_{Total} content. HRTEM images of particles parallel to cleavage were analyzed using Fast Fourier Transform to quantify the systematic layering distance of the particles.

We additionally constructed mineral stability diagrams for a simple Neoarchean ocean system. These were plotted in the Geochemist's Workbench (Bethke 2002) at a temperature of 25°C, and pressure of 1.013 bars. The solubility constant of greenalite (K_{sp}) was set to $10^{14.01}$, calculated from the Gibbs free energy of formation for greenalite estimated by Eugster and Chou (Eugster & Chou 1973). This K_{sp} is estimated for Fe(II)-greenalite rather than the low-Fe(III) greenalite that we observe – which does not have thermodynamic values available – but the stability lines for low-Fe(III) greenalite are expected to fall close to the plotted greenalite stability field. To simulate an ocean at silica saturation, the activity of $SiO_{2(aq)}$ was set to $10^{-2.71}$ M (Rimstidt & Barnes 1980). The fugacity of $CO_{2(g)}$ was set at 10^{-2} atm, after Halevy et al. (2017). We plotted the Eh vs. pH of this simplified ocean system with the Fe content set at 10^{-6} M to show stability fields for iron minerals within the stability limits of liquid water. To plot the Fe concentrations required to precipitate phases at variable pHs, the Eh was set to -0.2 V and ferrous iron was plotted from 10^{-8} to 10^{-2} M against pHs. Similar diagrams were constructed using oxygen fugacity ($f O_2$) to remove the pH dependence of the Eh axis and indicate the equilibrium O_2 constraints that greenalite represents. The highest $f O_2$ that formed stable greenalite rather than stable hematite (10^{-57} atm) was used in plotting Fe concentrations plotted against pH.

Results

Results from nanoscale, transmission-based results were corroborated using several different techniques on multiple scales. Microdrilled powders from a representative sample from Western Australia and South Africa were analyzed using X-ray diffraction (XRD) and X-ray absorption spectroscopy. XRD patterns were dominated by quartz, due to the unavoidable presence of the chert in the samples (Fig S1A). However, both samples additionally had two peaks coinciding with the most prominent diffraction peaks from a 7 Ångstrom clay mineral (Fig S1B); these reflections were distinguishable from ≥10 Ångstrom clay structures such as minnesotaite or stilpnomelane. The Western Australian sample, ABDP9 380.8 m, had diffraction peaks corresponding to ankerite and siderite in addition to peaks corresponding to a 7 Ångstrom clay.

We also examined the iron coordination environment in bulk powders using iron K-edge X-ray absorption near edge spectroscopy (Fe XANES). Consistent with its diffraction pattern, the Fe XANES of GKF 357.5 m had a spectral fingerprint similar to an iron silicate mineral (Fig S3). This spectrum had a prominent broad edge peak with a second distinctive peak at ~7142-7144 eV, similar to the spectrum of Fe-silicates such as greenalite and minnesotaite. However, the bulk Fe XANES of ABDP 380.8 m yielded a complex spectrum reflecting a mixture between Fe-silicate and Fe-carbonate (Fig S3). To target only nanoparticle-rich chert without interference from other Fe-bearing compounds, it was necessary to use microscale and nanoscale rather than bulk techniques.

Therefore, we additionally analyzed the iron silicate nanoparticle mineralogy at a microscale using Fe XANES. We collected spectra from ~3x3 µm spots throughout typical chert subregions in thin sections from the two representative samples analyzed in bulk (ABDP9 380.8 m and GKF 357.5 m) along with three additional thin sections through BIF- and carbonate-hosted ferruginous cherts (ABDP9 222.7 m, GKF 356.6 m, and DDH44 388.3 m). Regions of compacted microcrystalline (< 20-30 µm granules) chert

and coarser quartz crystals (20-50 μm, "mesocrystalline quartz" in Maliva et al, 2005) cemented by silica were targeted using light microscopy, avoiding veins or large cross-cutting secondary minerals if possible (Fig S2). These areas were mapped using iron x-ray fluorescence (XRF) and appeared to have a low background of iron, representing the disperse nanoparticle inclusions in chert that do not individually show up at our ~3 μm resolution (Fig S2). The Fe XRF maps were used to guide the positions of 3x3 μm point spectra, which represented the average Fe XANES from disseminated 10nm – 500nm nanoparticles—approximately 30-150 particles on the surface depending on the variable particle density with some contribution from deeper particles. Spectra from all five of these thin sections appeared extremely similar to each other, and resembled the greenalite and minnesotaite standard spectra (Fig S3). Notably, iron was extremely low in silica cements that surrounded the coarser quartz euhedra, confirming that the iron silicate nanoparticles were original to the early chert preciptiation and later cementing fluids did not contain iron silicates.

The pre-edge features of these microscale Fe XANES of iron inclusion-bearing chert can also be examined for the relative iron redox state. The pre-edge features of the nanoparticle spectra suggested that there was very little Fe(III) and that the iron silicate particles are dominated by Fe(II) (Fig S5).

The iron redox state of the nanoparticles was also examined using STXM-based analyses of the Fe L-edge. In addition to acquiring multiple energy maps that could be converted into $Fe(III)/Fe_{Total}$ maps, we also gathered image stacks from a subregion of each FIB foil. These enabled us to derive an average Fe L-edge spectrum from areas containing approximately 10-30 particles from each sample foil (Fig S6). The calculated average $Fe(III)/Fe_{Total}$ from each of these samples ranged from ~13-20% (Fig S6, Table S1).

To explore the stable solution chemistries and redox space predicted by the presence of primary greenalite, we constructed stability diagrams using Geochemist's Workbench (Figure S7). Early inclusions of greenalite predict an extremely low Eh, or oxidation potential, of the Neoarchean ocean (Figure S7A). The presence of greenalite as a primary Neoarchean mineral is not consistent with an oxidizing, or oxygenated, ocean, but rather imply an ocean Eh of <0.1 V and likely far lower–corresponding to an oxygen fugacity ($f\,O_2$) < 10^{-56} atm (Figure S7C). Greenalite also constrains the Neoarchean ocean pH to >5.5 (consistent with estimates (Halevy & Bachan 2017)). In addition, iron concentrations need only reach 30 nM to favorably precipitate greenalite. As suggested previously (Tosca et al. 2016), Figure S7B and D clearly demonstrate how greenalite would set the upper range of ferrous iron in the oceans and regulate the iron cycle of early oceans.

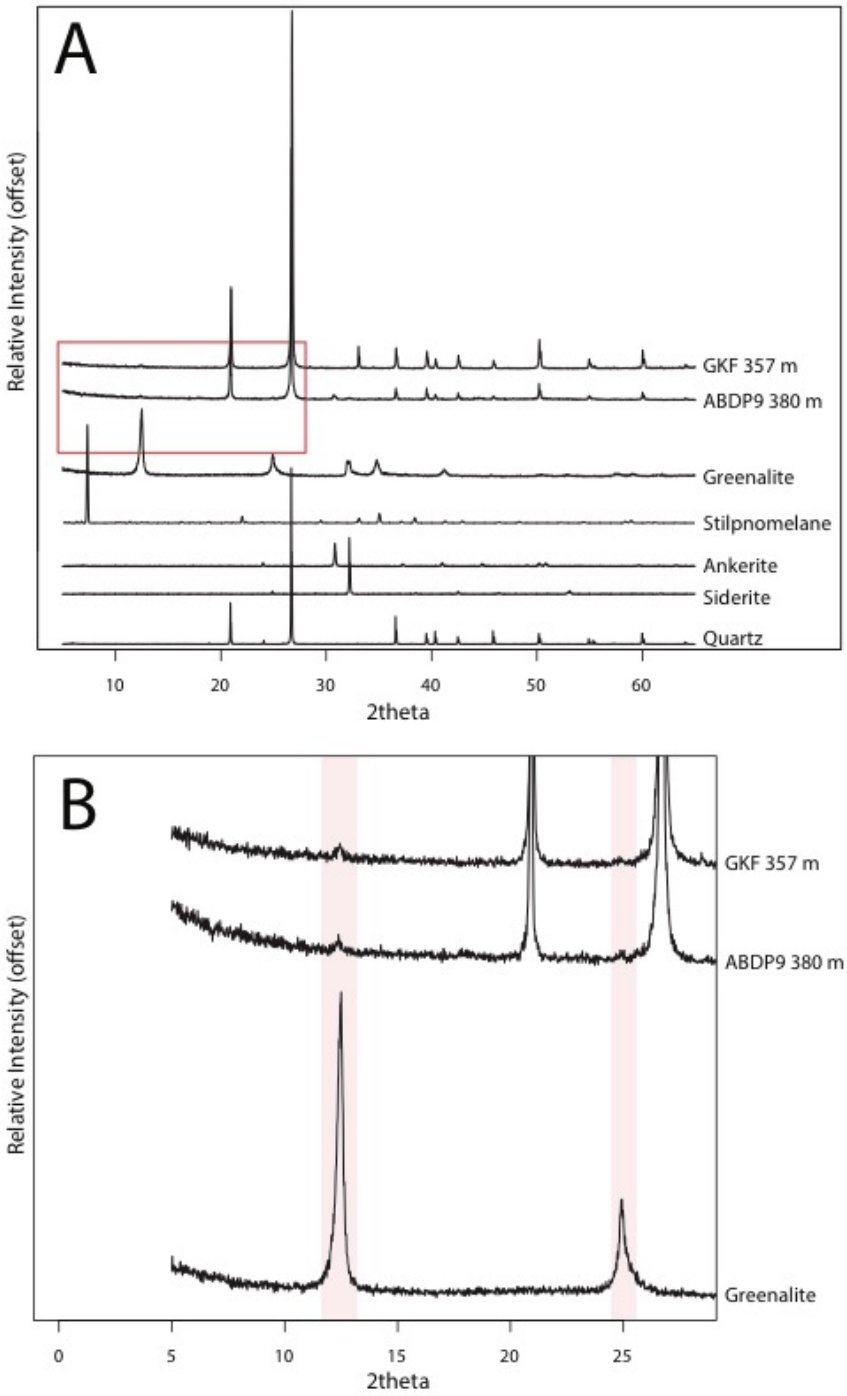

Figure S1:
A. Bulk X-ray diffraction of microdrilled samples GKF 357 m and ABDP9 380 m compared to standards. B. Zoom of two small sample peaks at small 2theta characteristic of clay minerals (with 7 Ångstrom d-spacings).

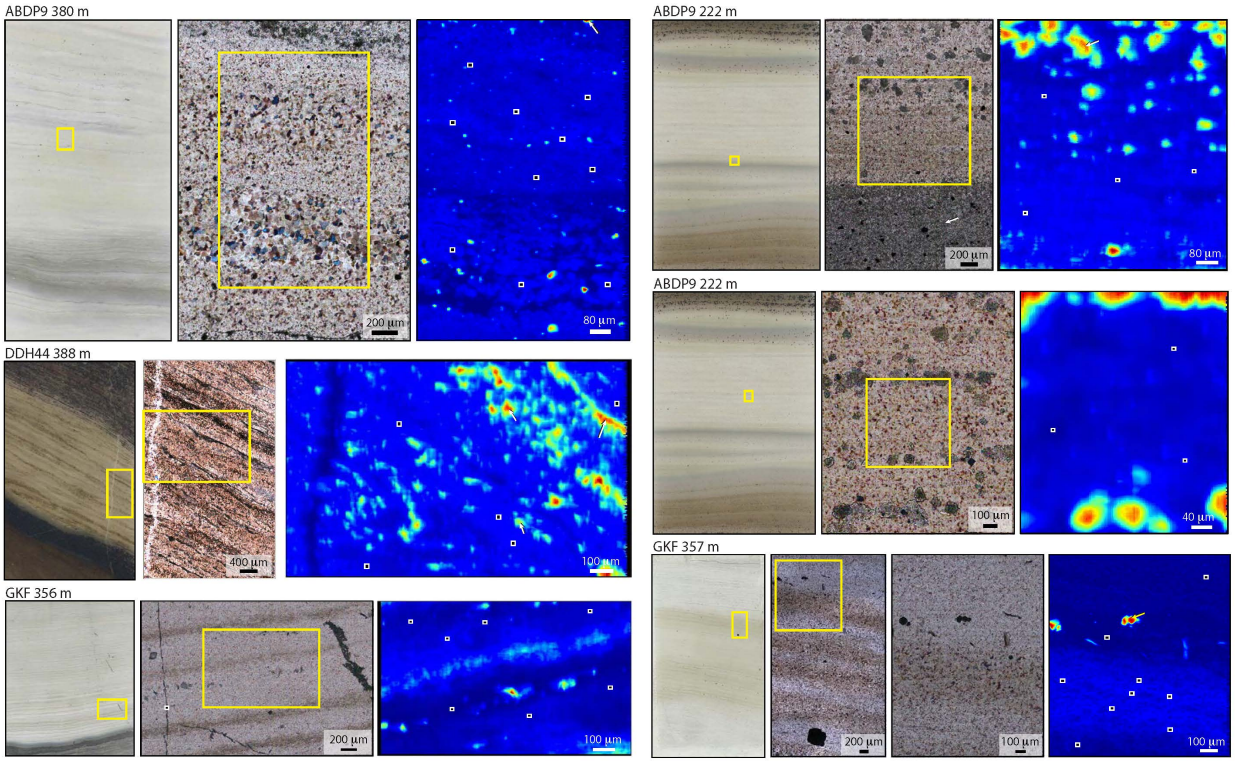

Figure S2:
Thin section photos and optical transmission images indicating positions of adjacent iron X-ray fluorescence maps acquired at 8000 eV or 11,000 eV. Black rectangles with white borders indicate positions of Iron X-ray Absorption Near Edge Spectroscopy (Fe-XANES) point spectra of "background" iron in chert, targeting disperse iron-rich inclusions in chert. White arrows indicate positions of Fe-XANES point spectra of larger high-iron minerals.

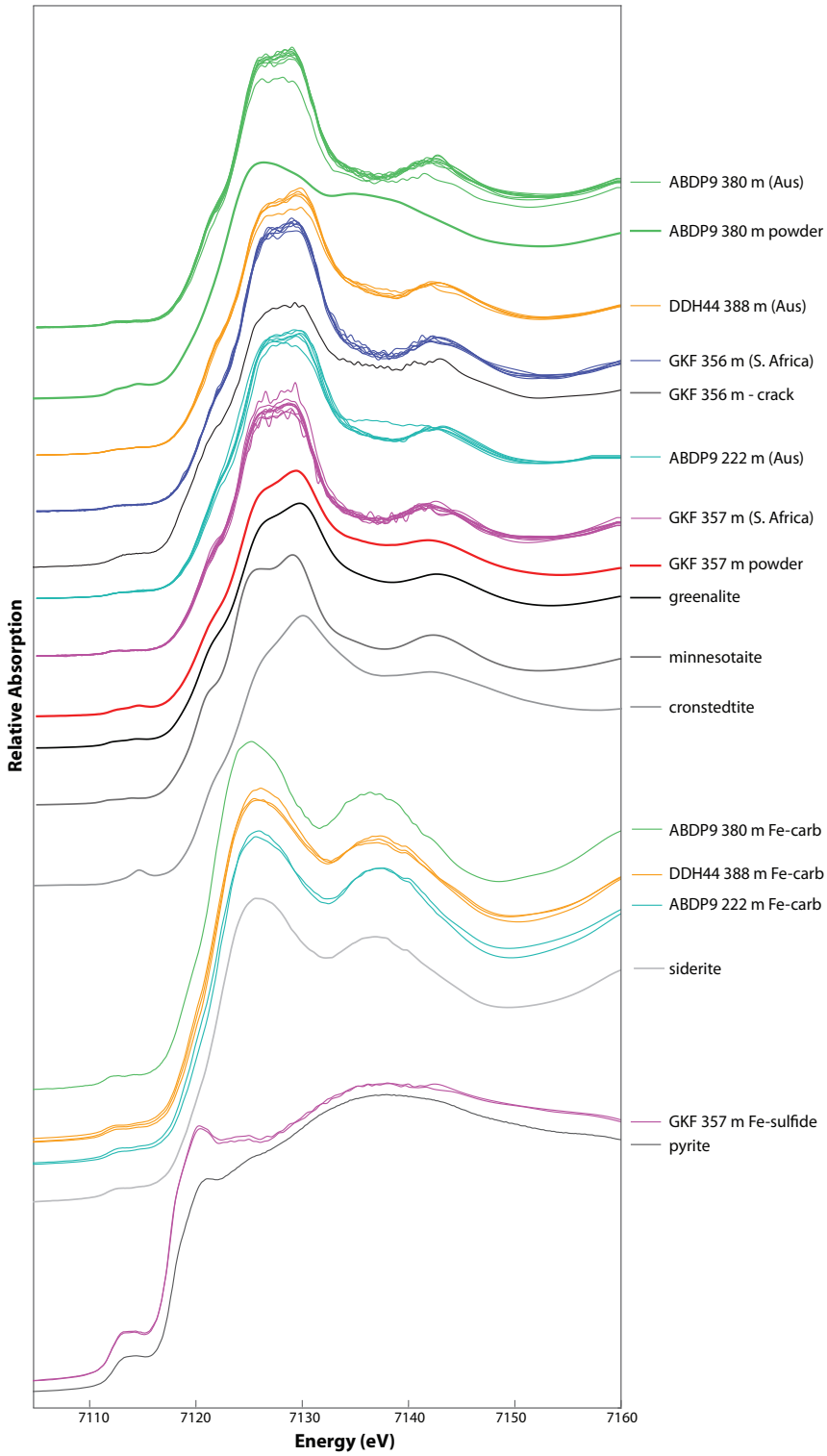

Figure S3:
Iron X-ray Absorption Near Edge Spectroscopy (Fe-XANES) point spectra from thin sections (positions shown in Figure S2) compared to iron standard minerals. “Background” iron in chert is most consistent with an iron silicate such as greenalite or minnesotaite, while high-iron minerals are spectrally fingerprinted to be siderite and pyrite.

Figure S4:

A. ABDP9 219 m

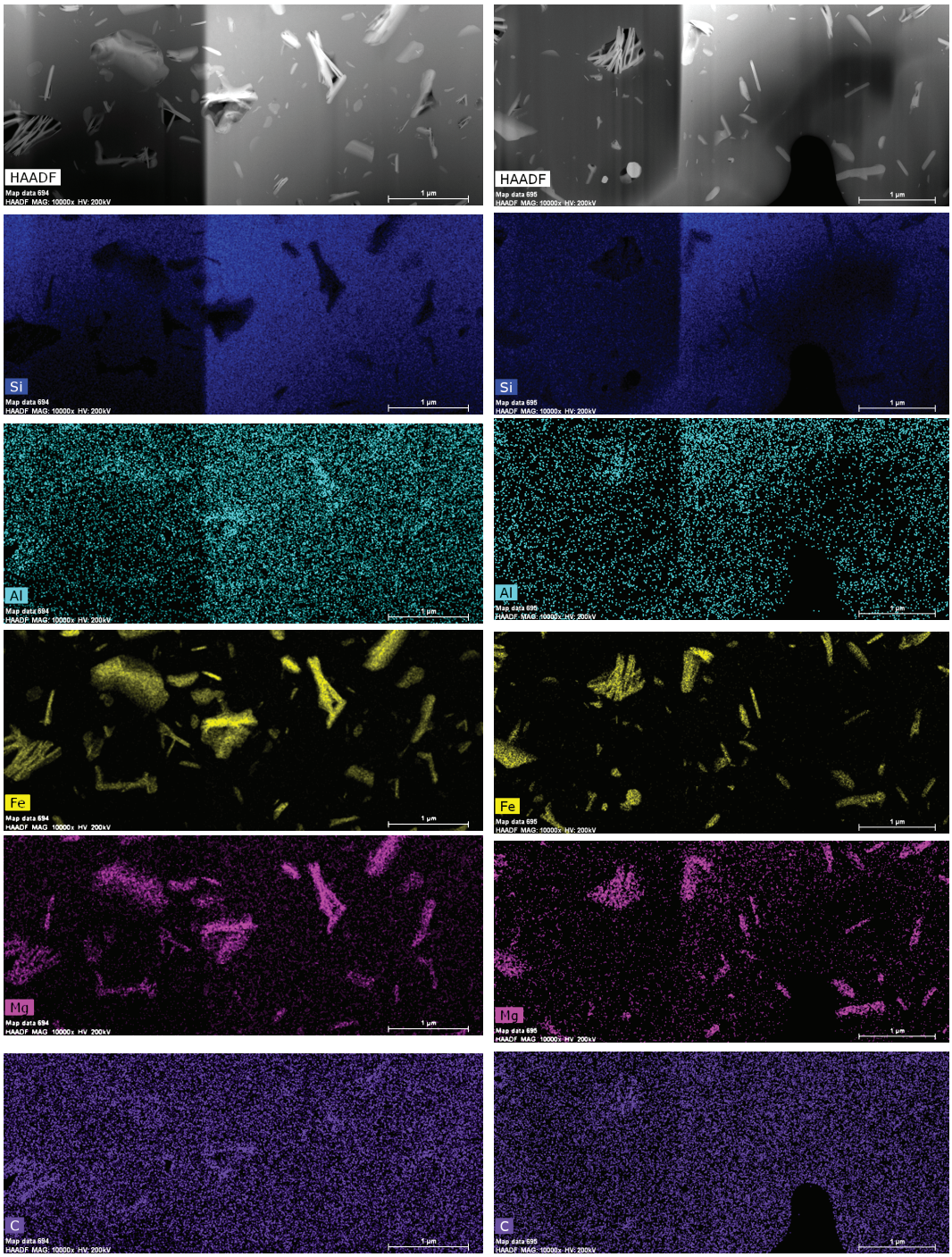

Scanning Transmission Electron Microscopy (STEM) images of ABDP9 219 m shown on top row, with elemental maps of Si, Al, Fe, Mg, and C acquired from qualitative Energy Dispersive Spectroscopy (EDS) mapping on the TEM.

B. GKF 327 m

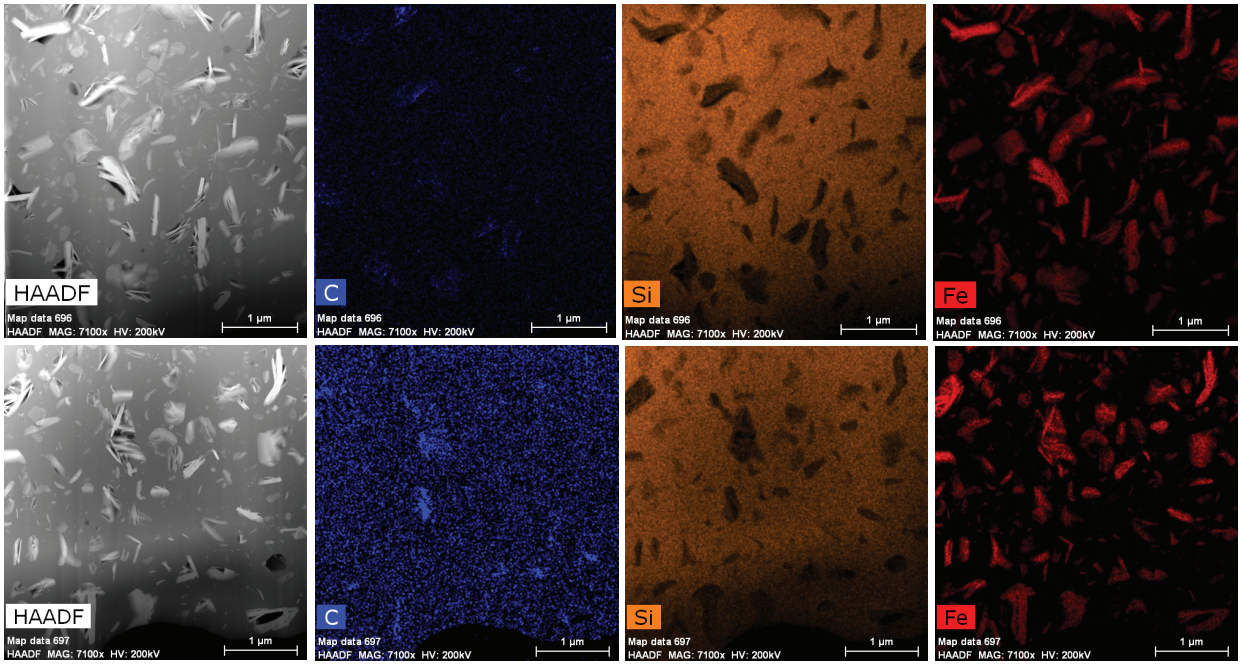

Scanning Transmission Electron Microscopy (STEM) images of GKF 327 m shown on left, with elemental maps of C, Si, and Fe acquired from qualitative Energy Dispersive Spectroscopy (EDS) mapping on the TEM.

C. ABDP9 288 m1

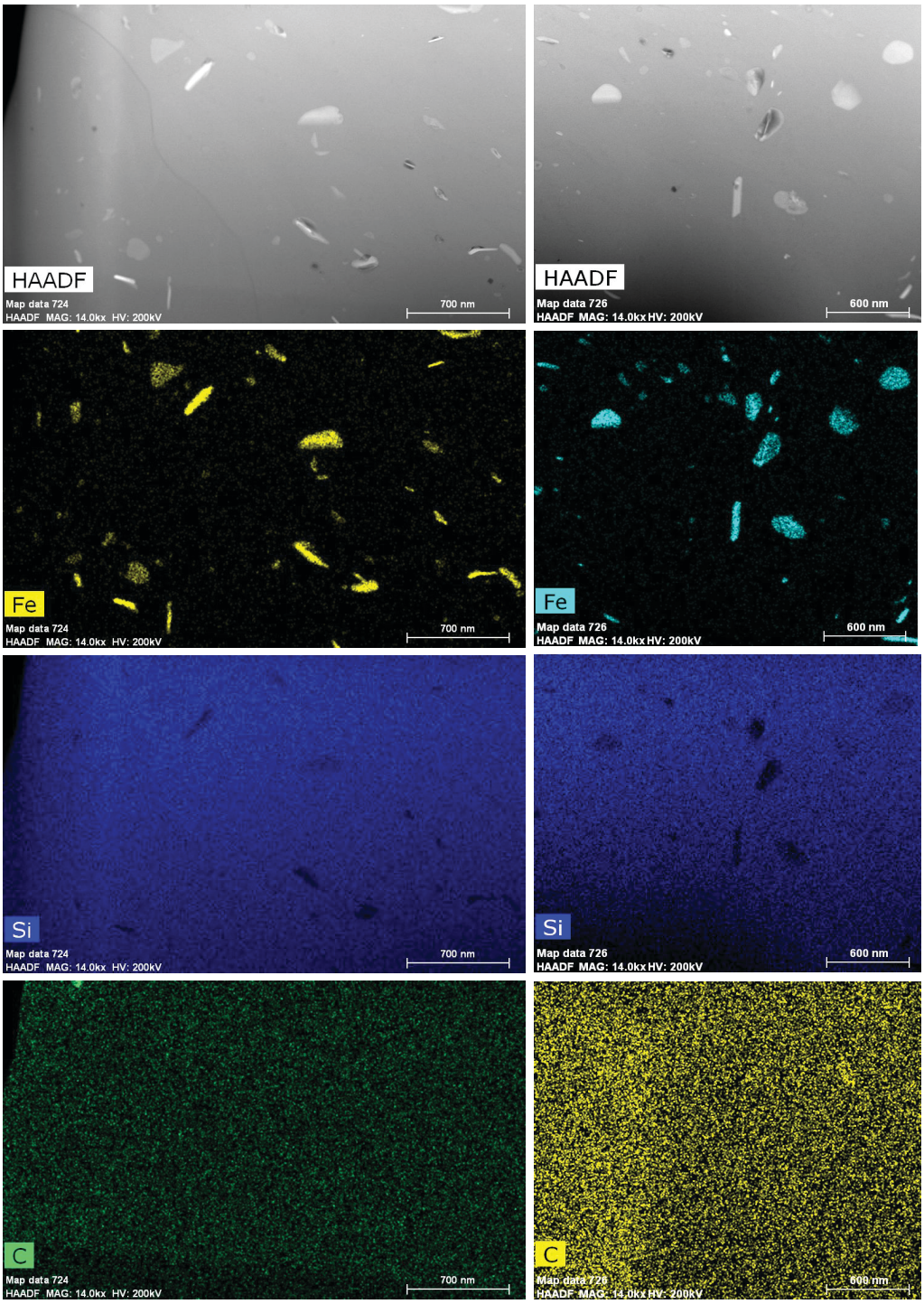

Scanning Transmission Electron Microscopy (STEM) images of ABDP9 288 m1 shown on top row, with elemental maps of Fe, Si, and C acquired from qualitative Energy Dispersive Spectroscopy (EDS) mapping on the TEM.

D. ABDP9 288 m2

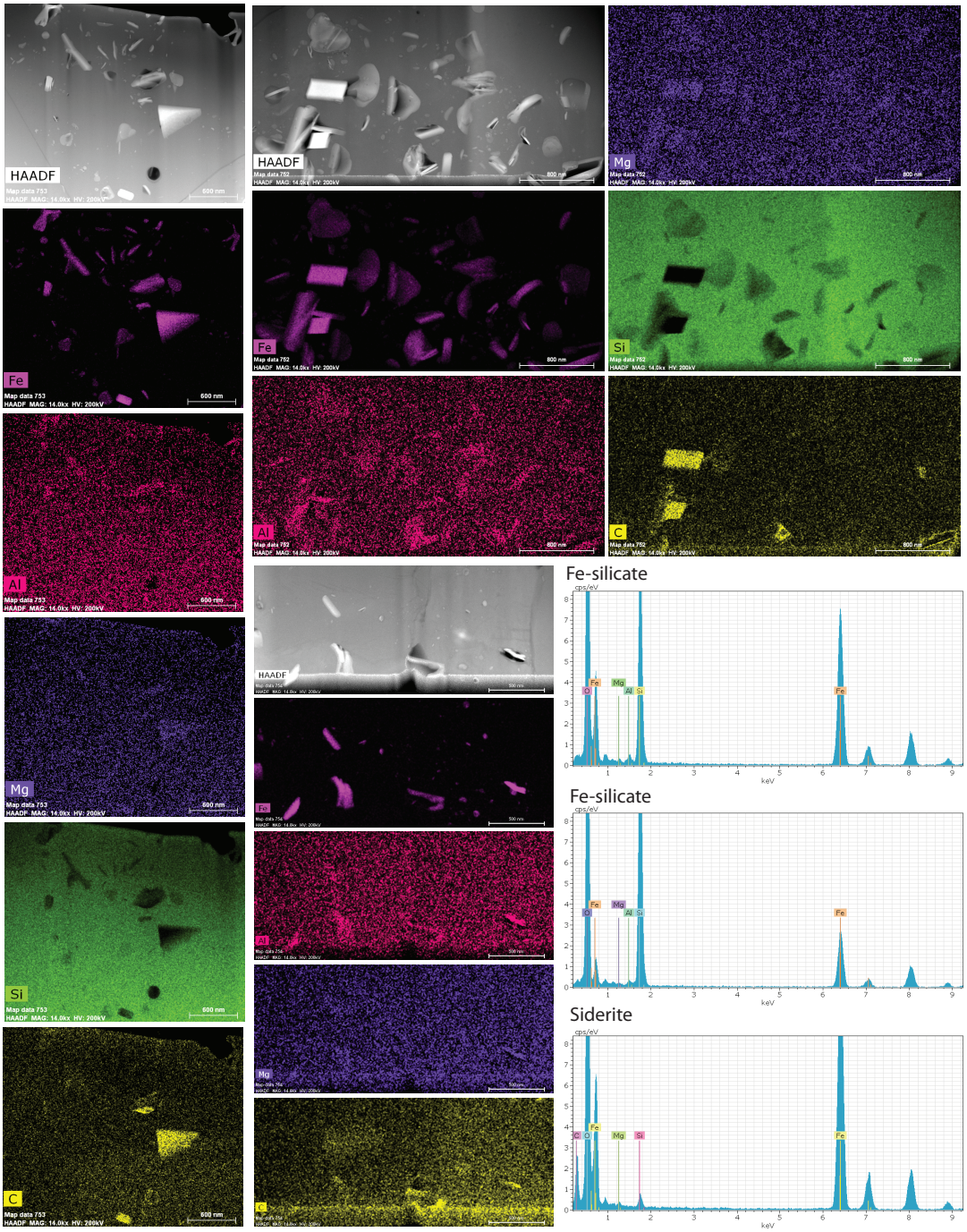

Scanning Transmission Electron Microscopy (STEM) images of ABDP9 288 m2 shown alongside corresponding elemental maps of Fe, Al, Mg, Si, and C acquired from qualitative Energy Dispersive Spectroscopy (EDS) mapping on the TEM. Two EDS spectra are shown from particles that did not contain significant carbon and appear to be mainly comprised of Fe, Si and O – suggesting these are some form of iron silicate. One EDS spectra from a particle with high C is also presented, and the lack of Si and high Fe, C, and O suggests these particles are siderite.

E. Silv 313 m

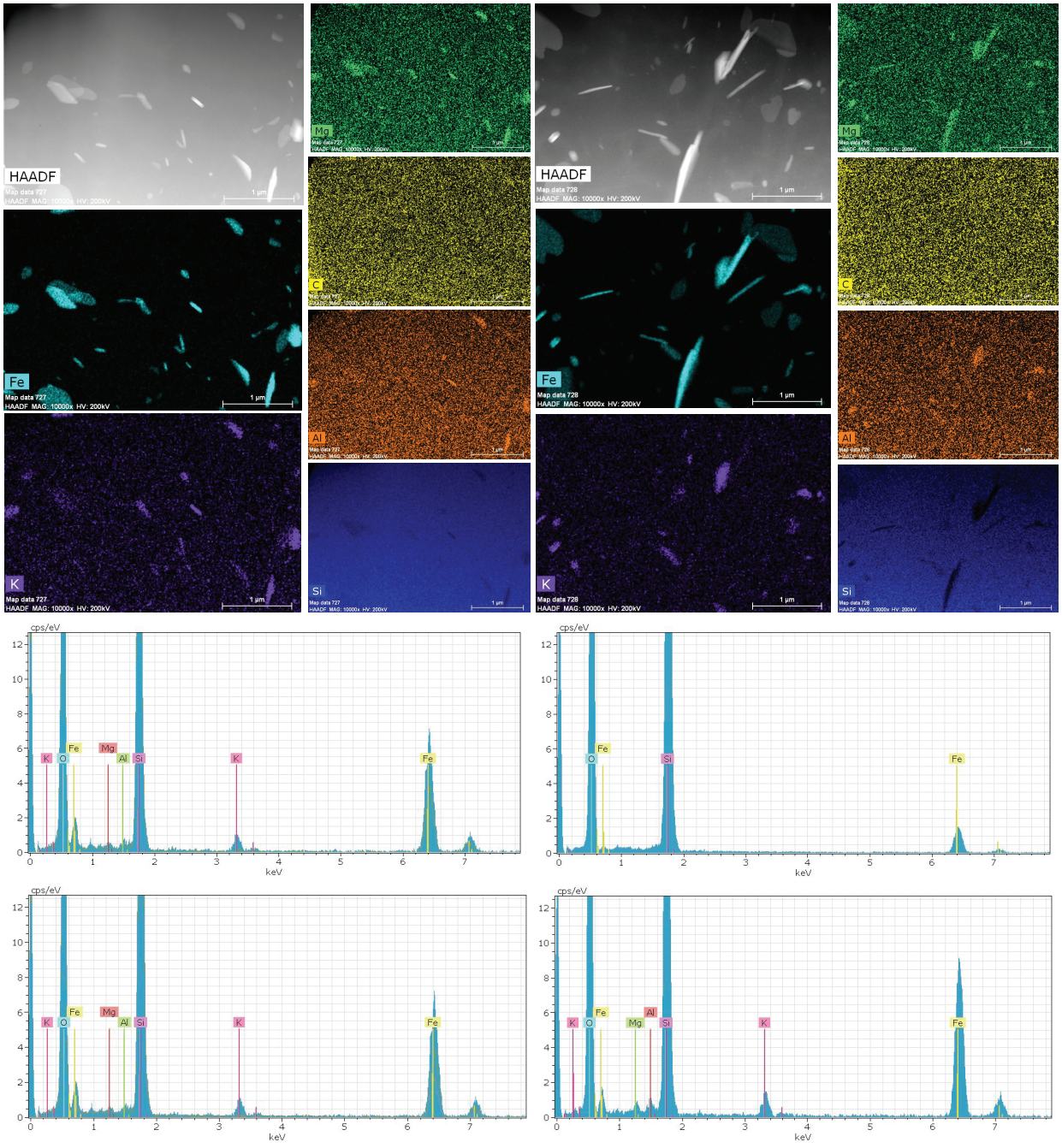

Scanning Transmission Electron Microscopy (STEM) images of Silv 313 m shown on top left, alongside corresponding elemental maps of Fe, K, Mg, C, Al, and Si acquired from qualitative Energy Dispersive Spectroscopy (EDS) mapping on the TEM. Two minerals appear to be present from their contrasting elemental signatures. Three EDS spectra from the K-bearing mineral are shown below, which also has higher Al and Mg. One EDS spectra from a particle without high K is shown on the upper right and only has measurable Fe, Si, and O.

Table S1:

All elements	Point 1	Point 2	Point 3	**greenalite Fe3Si2O5(OH)4**
Si	17.48	16.21	16.68	**15.1**
Al	0.51	0.66	0.87	
Fe	41.09	39.75	39.01	**45.1**
O	40.91	43.37	43.44	**38.7**
TOTAL (norm)	99.99	99.99	100.00	**371.70**

Energy dispersive X-ray spectrometry analyses on several particles from GKF 327.2, normalized to 100, as compared to the weight % distribution among elements in ideal greenalite. These values are consistent with the greenalite identification of the nanoparticles, with slight excess in Si and O possibly due to the surrounding chert and/or water contamination. Analyses were quantified using the Bruker ESPRIT software and the Cliff-Lorimer correction procedure.

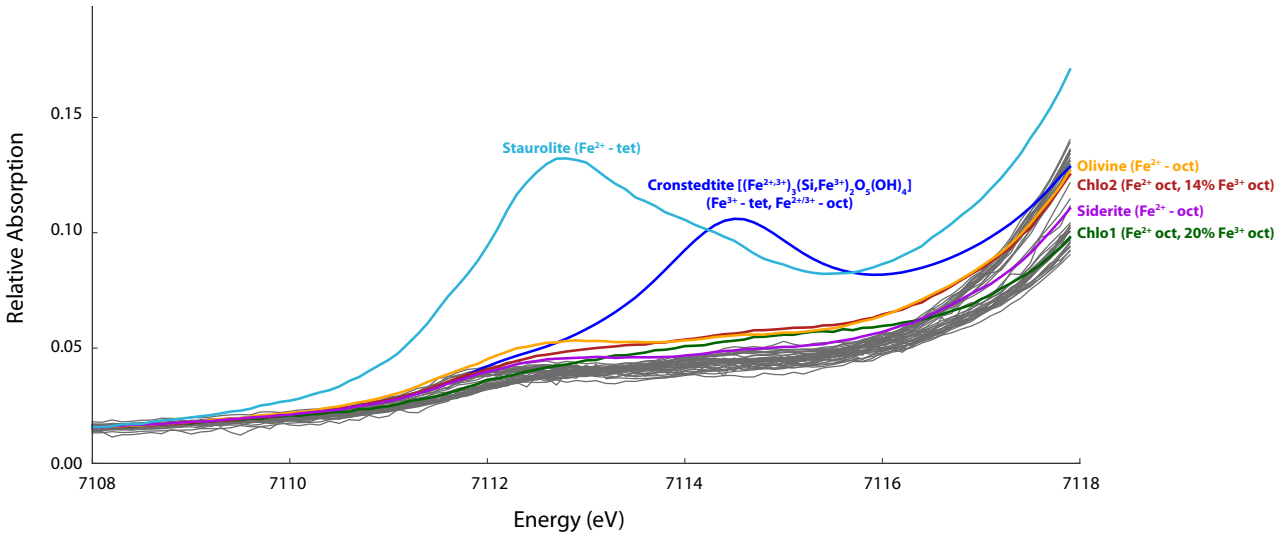

Fig S5:

The Fe K-edge pre-edge feature is useful for understanding redox state and coordination environment of Fe. Nanoparticles (Fe "background" in chert) from each thin section are plotted in gray, and are comparable to standards for Fe(II) in octahedral coordination in olivine and siderite, Fe(II) and Fe(III) octahedrally coordinated in chlorite standards with 14-20% Fe(III). The nanoparticle pre-edges contrast with tetrahedrally coordinated Fe(II) in a staurolite standard and the Fe(III)-rich 2-layer silicate cronstedtite. These measurements are consistent the nanoparticles having low Fe(III)/Fe_{Total}.

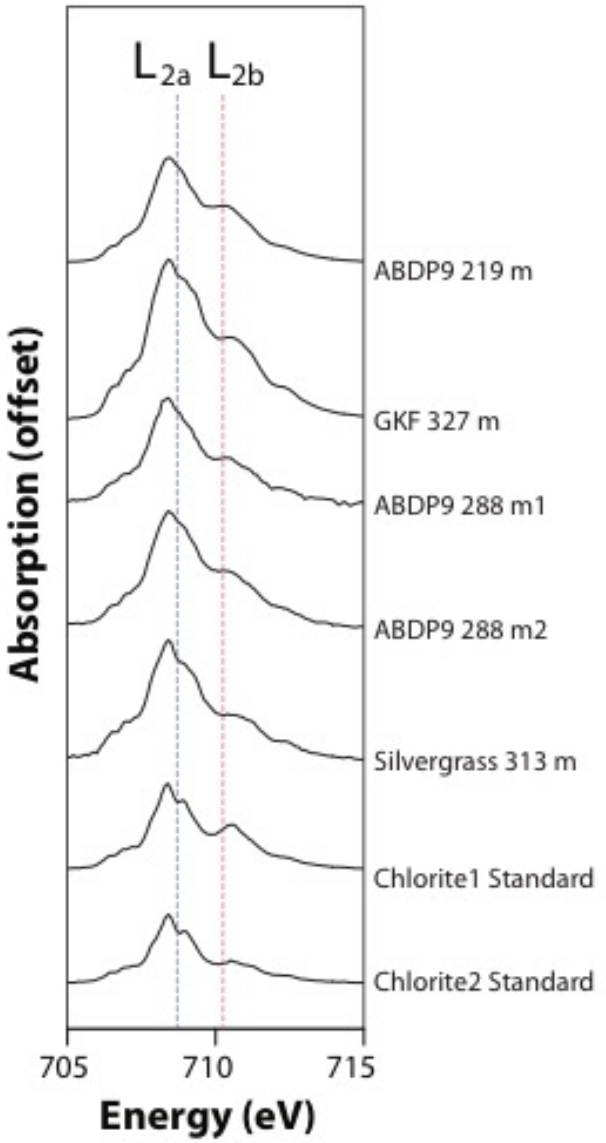

Fig S6:

L-edge X-ray absorption spectra of Fe, averaged across particles from a subregion of each sample FIB foil. The ratio of L_{2b}/L_{2a} can be used to quantify Fe^{3+} content using an iron silicate calibration established by Bourdelle et al (2013). For ease of comparison, ABDP9 288 m1 was vertically multiplied by 3 and ABDP9 288 m2 was vertically multiplied by 1.5. Also shown are chlorite standards measured during the same beam time as internal standards. Analytical results from these spectra are presented in Table S2.

Table S2:

Standard/sample	% Fe(III) calculated	Actual, if known
Chlorite1 standard	20.6	20
Chlorite2 standard	9.8	14
ABDP9 219 m	20.2	
GKF 327 m	18.6	
ABDP9 288 m1	15.7	
ABDP9 288 m2	17	
Silv 313 m	12.7	

Fe(III) content calculated from Fe L-edge spectra acquired by averaging a subregion of particles for each sample; also shown are internal calibration standards with their known Fe(III) values.

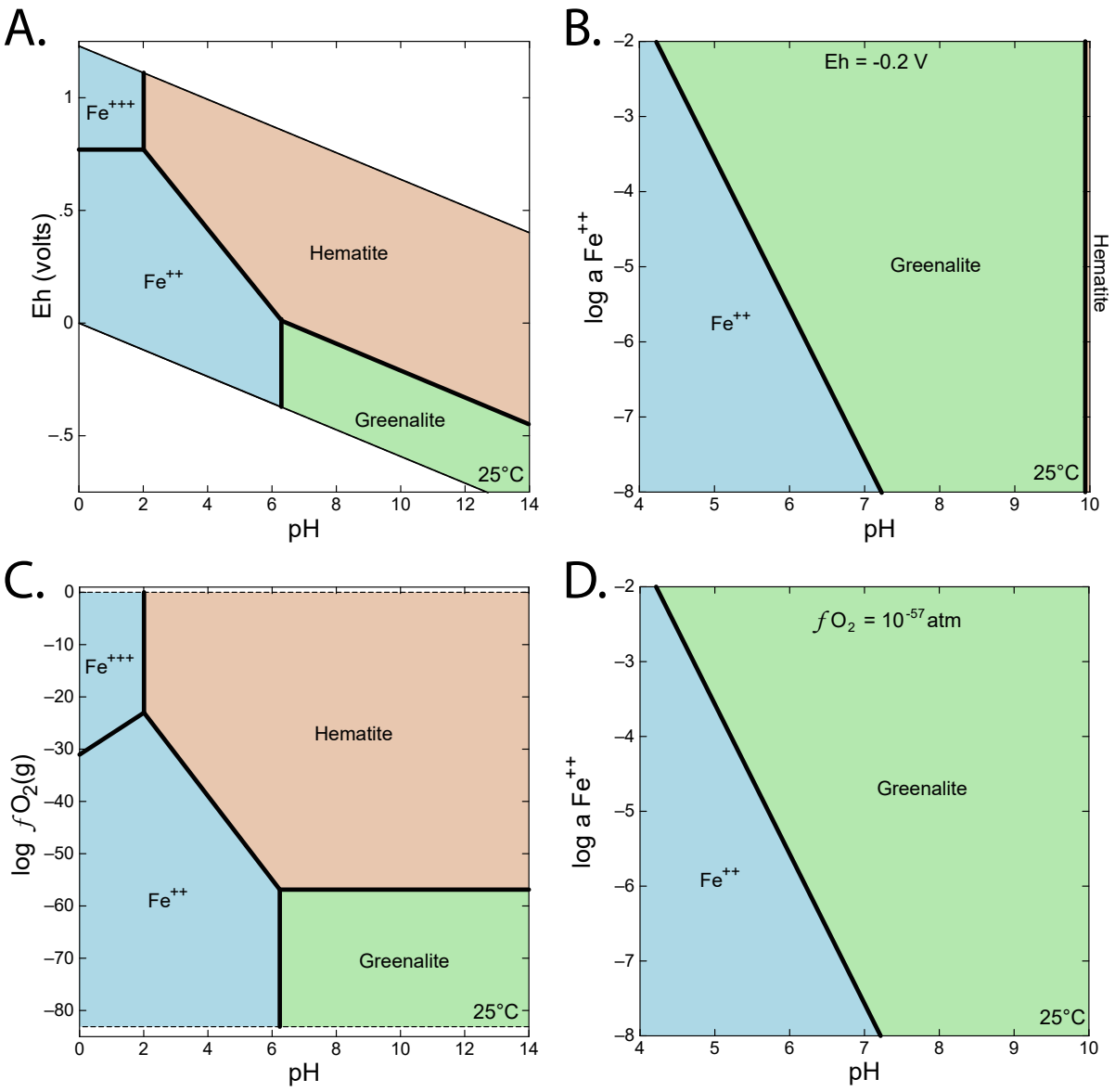

Fig S7:

Mineral stability diagrams for iron made in Geochemist's Workbench, with $[SiO_2]_{(aq)}$ set to $10^{-2.71}$ M (amorphous silica saturation) and $[CO_2]_{total}$ set to 10^{-2} M. A. Eh vs. pH with boundaries set by the stability of water and Fe^{2+} = 10^{-6} M. Solid lines constructed using solubility constant for greenalite calculated from Eugster and Chou (1973). B. The activity of Fe^{2+} plotted against pH at a set Eh = -0.2. Greenalite has a large stability field in this chemical space, and hematite would also be predicted to form at high pHs > ~10. C. Mineral stability diagram plotted by the fugacity of oxygen (f O_2) vs pH. The stability field of greenalite encompasses a large pH range but constrains f O_2 to < 10^{-56} atm. D. The activity of Fe^{2+} plotted against pH at f O_2 = 10^{-57} atm.